# Observation of Wave Energy Evolution in Coastal Areas Using HF Radar

RAFAEL J. RAMOS, HANS C. GRABER, AND BRIAN K. HAUS

*Applied Marine Physics Department, Rosenstiel School of Marine and Atmospheric Science, University of Miami, Coral Gables, Florida*

(Manuscript received 5 February 2008, in final form 30 January 2009)

ABSTRACT

The capability of phased-array HF radar systems to sample the spatial distribution of wave energy is investigated in different storm scenarios and coastal configurations. First, a formulation introduced by D. E. Barrick to extract significant wave height $H_s$ from backscatter Doppler spectra was calibrated and subsequently tested (to assess bias and uncertainty) with data from seven different buoy/gauge stations collected during three different field experiments. Afterward, $H_s$ observations were obtained for selected sampling locations within the radar effective domain (in all experiments), and a filtering technique based on wavelet transform characterization and decomposition was applied. The accuracy of the filtered radar-derived observations was assessed by comparing these estimates to results from independently calibrated wave propagation models. It was found that the HF radar accurately measured the energy field induced by different storm events. The filtering technique minimized the contribution of unrealistic features introduced by the presence of defective sampling, which is intrinsic to radar remote sensing at this frequency, and it proved to be central for the use of the HF radar as a tool to identify wave energy trends and potential zones of wave energy concentration in coastal areas. These findings show that the sampling capabilities of radar systems may be greatly enhanced because reliable wave energy estimates can be obtained in addition to conventional surface current measurements. This is particularly important in locations such as harbor entrances where in situ measuring devices cannot be deployed.

## 1. Introduction

Although methods have been developed to extract wave energy properties from radar measurements, their application to studies of the energy field within the entire radar domain has been limited for various reasons. Most methods have not been extensively validated and the few that have been are only applicable under very restrictive conditions. Additionally, the high variance of the radar observations produced by such methods has required considerable spatial and temporal averaging. Previous work in this field has focused on showing the change of wave energy quantities in the presence of atmospheric disturbances such as easterly winds and low pressure systems (Graber and Heron 1997; Wyatt 1997) and limited point comparisons among buoy measurements, radar estimates, and even wave model estimates (Wyatt et al. 2003), mostly for validation purposes. It was only very recently that radars had been used as a tool to study wave–current interaction (Haus et al. 2006) and the effects of current shear on fetch-limited wave growth (Haus 2007). This work addresses the validity of HF radar measurements under wave energy growth and attenuation conditions and establishes the limitations of the technique in terms of noise contamination of the backscatter signal. It is shown that, by properly filtering deficient samples, an effective range for radar wave measurements can be defined.

The remainder of this section introduces the method to estimate significant wave height $H_s$ and the supplementary filtering technique. Section 2 presents an overview of the experimental venues and the collected data. Section 3 addresses the calibration and validation of the $H_s$ observations, including the establishment of range limitations. Section 4 presents the comparisons of filtered and unfiltered radar-derived estimates with their theoretical counterpart for different cases of wave energy attenuation, growth, and variations resulting from wave–current interaction. Finally, conclusions are drawn in section 5.

*Corresponding author address:* Rafael J. Ramos, Applied Marine Physics Dept., Rosenstiel School of Marine and Atmospheric Science, University of Miami, 4600 Rickenbacker Causeway, Miami, FL 33149.
E-mail: rramos@rsmas.miami.edu

DOI: 10.1175/2009JTECHO631.1

# Report Documentation Page

*Form Approved*
*OMB No. 0704-0188*



| 1. REPORT DATE | 2. REPORT TYPE | 3. DATES COVERED |
|---|---|---|
| **SEP 2009** | | **00-00-2009 to 00-00-2009** |

| 4. TITLE AND SUBTITLE | 5a. CONTRACT NUMBER |
|---|---|
| **Observation of Wave Energy Evolution in Coastal Areas Using HF Radar** | 5b. GRANT NUMBER |
| | 5c. PROGRAM ELEMENT NUMBER |
| 6. AUTHOR(S) | 5d. PROJECT NUMBER |
| | 5e. TASK NUMBER |
| | 5f. WORK UNIT NUMBER |
| 7. PERFORMING ORGANIZATION NAME(S) AND ADDRESS(ES) **Applied Marine Physics Department,Rosenstiel School of Marine and Atmospheric Science,University of Miami,Coral Gables,FL** | 8. PERFORMING ORGANIZATION REPORT NUMBER |
| 9. SPONSORING/MONITORING AGENCY NAME(S) AND ADDRESS(ES) | 10. SPONSOR/MONITOR'S ACRONYM(S) |
| | 11. SPONSOR/MONITOR'S REPORT NUMBER(S) |

12. DISTRIBUTION/AVAILABILITY STATEMENT
**Approved for public release; distribution unlimited**

13. SUPPLEMENTARY NOTES

14. ABSTRACT

15. SUBJECT TERMS

| 16. SECURITY CLASSIFICATION OF: | | | 17. LIMITATION OF ABSTRACT | 18. NUMBER OF PAGES | 19a. NAME OF RESPONSIBLE PERSON |
|---|---|---|---|---|---|
| a. REPORT | b. ABSTRACT | c. THIS PAGE | | | |
| **unclassified** | **unclassified** | **unclassified** | **Same as Report (SAR)** | **19** | |

### a. Estimation of significant wave height

Ocean remote sensing using HF radar is based on the measurement of the backscattered power from emitted radar waveforms. Because the electromagnetic waves scatter from moving surface waves, a Doppler shift in the emitted frequency is induced and recorded at the receiving antenna. The Fourier transform (FT) of the recorded backscatter power (covariance) expressed as a function of Doppler frequency is known as the Doppler spectrum. The background structure in the Doppler spectrum away from the resonance regions is a function of the sea state.

The first comprehensive theory of HF radar waveform scattering from the ocean surface was introduced by Barrick in the early 1970s (Barrick 1971a,b,c, 1972). Based on the theory of vertically polarized electromagnetic signals approaching at near-grazing incidence angles and scattering from random rough surfaces, Barrick derived expressions to estimate the first-order (Bragg peaks) and background high-order peak structures (to the second order) of the Doppler spectrum. In a later work, following a simplification of this theory, Barrick (1977a,b) introduced expressions to estimate the root-mean-square (RMS) wave height $H_{\rm rms}$ and mean wave period $\overline{T}$ as a function of the backscatter power ratio of the second-order to first-order regions of the Doppler spectrum. Accordingly, the significant wave height is given by

$$H_s = \frac{2^{5/2}\alpha}{k_o}\left\{\frac{\int_{-\infty}^{\infty}[\sigma_{(2)}(f_d)/W(f_d)]\,df_d}{\int_{-\infty}^{\infty}\sigma_{(1)}(f_d)\,df_d}\right\}^{1/2}, \qquad (1)$$

where $\alpha$ is a correction factor, $k_o = 2\pi f_o C^{-1}$ is the radar wavenumber, $f_o$ is the radar frequency (frequency of the radar waveform), $C$ is the speed of the electromagnetic waves ($C = 3 \times 10^8$ m s$^{-1}$), $f_d$ is the Doppler frequency, $\sigma_{(1)}$ and $\sigma_{(2)}$ are the first- and second-order average radar cross section (RCS) per unit (mean) sea surface area (ordinates of the Doppler spectrum), and $W$ is a weighting function that accounts for hydrodynamic and electromagnetic wave coupling. The factor $\alpha$ is introduced to correct for biases in the estimates because of simplifications in the theory and other radar-dependent factors and should also account for a weak dependence of $W$ on the radar-look angle that was not fully removed during the corresponding derivation process. The correction factor $\alpha$ must be determined empirically.

It should be mentioned that other simplified formulations based on Eq. (1) have been introduced in related literature (Maresca and Georges 1980; Heron et al. 1985). They express $H_s$ as a function of the ratio of unweighted second-order to first-order backscatter power of the Doppler spectrum. However, the exclusion of $W$ in such formulations results in higher directional variability and lower coverage because they are prone to provide significant errors near crosswind conditions.

Previous performance comparisons of the aforementioned methodologies with a limited subset of the data presented in this work confirmed that Eq. (1) produces more accurate results (Heron and Heron 1998). However, further analysis of the numerical scheme used (for other storm systems and higher sea states) showed that Eq. (1) produced adequate estimates for low sea states but significantly overestimated the values in the range $H_s > 2.97$ m (Ramos 2006). This tendency was found to be mostly related to the inability of the scheme to account for width variations of the first-order peak, as the first- and second-order limits of the Doppler spectrum were fixed and imposed a priori. To address this shortcoming, the scheme proposed in this study defines the first- and second-order limits as the nulls (minimum values) in the range $(2 - 2^{1/2})f_B \le f_d \le 2^{1/2}f_B$, where $f_B = (2\pi^2)^{-1/2}(gk_o)^{1/2}$ is the Bragg frequency and $g$ is the acceleration of gravity. The boundary values in the selected range are associated to resonance of the second harmonic of $k_o$. Results of the corresponding validation are discussed in section 3.

### b. Filtering technique

The accuracy of radar-derived $H_s$ observations is highly dependent on the shape of the recorded Doppler spectrum. However, several factors such as range (distance) and scattering strength of the targeted ocean patch, temporary obstructions, variations in levels of radio frequency interference (RFI), and extraneous electromagnetic signals can significantly affect the structure of the second-order region of the Doppler spectrum, causing it to deviate from its ideal shape and therefore from the assumptions used for the derivation of Eq. (1). Because some of these factors are inherent to radar sampling, the observations are, by nature, highly scattered. In addition, time series outliers caused by one or a combination of the aforementioned factors tend to cluster in time and space, which makes it difficult to remove them with conventional smoothing techniques. Thus, a distinctive filtering methodology based on wavelet analysis (characterization and reconstruction) was introduced for the treatment of the data.

Wavelet analysis can be used to extract information from a random process and has been used successfully in the determination of periodicity and frequency changes and their time localizations in the following: climate time series (Lindsay et al. 1996; Liu and Miller 1996; Markin 1995; Torrence and Compo 1998), the study of wave grouping and growth (Liu 1994; Ramos 2001), and

other special applications such as the analysis of directional properties of wave spectra (Donelan et al. 1996). However, wavelet analysis can be also used as a basis to isolate selected properties of a random process through decomposition, reconstruction (synthesis) and filtering (Haus et al. 2004). The advantage over its Fourier counterpart (apart from not imposing periodicity constraints) is the possibility of local characterization, which allows the analysis and synthesis of a signal segment using a limited range of frequencies (scales). Furthermore, it is possible to isolate the domain (in time and frequency) affected by irregularities in the data and use analysis results outside this region, which are reliable regardless of the data quality in the affected segment.

The wavelet analysis (continuous domain) of a function is based on its continuous wavelet transform (CWT), which involves the convolution of the given function (or data series) and a series of shifted and scaled versions of another function called the mother or analyzing wavelet. The result of this operation is a set of coefficients that can be associated with energy content and that can be further related to frequency and time, depending on the scale and shift of the mother wavelet. The scale (frequency) domain may be conveniently discretized in intervals of logarithmic (base 2) increments so that features with different lengths can be analyzed simultaneously and with different levels of detail. The mother wavelet of choice in a particular case depends on the nature of the data series to be analyzed and on the characteristics of the phenomenon that need to be resolved from that series. Several complex and real-valued mother wavelets with different widths and shapes have been defined and are available in related literature (see compilation by Foufoula-Georgiou and Kumar 1994). For the analysis presented in this work, the second derivative of Gaussian wavelet (DOG2), also known as the Mexican hat, was chosen because it provided a better time localization of the storm events than other widely used wavelet functions, such as Morlet. The advantage of DOG2 comes from the fact that the shape (time domain) of the DOG2 wavelet better fits the representation of storms, which is characterized by a single cycle of increase and decrease of wave energy as they propagate through a fixed measuring location.

By definition, the discrete form of the CWT of the function $y(t)$ is given by (Ramos 2006)

$$\tilde{Y}_n(s) = \sum_{m=1}^{N} \frac{\hat{Y}_m}{N} \Psi^*(sf_m) \exp\left[\frac{i2\pi(m-1)(n-1)}{N}\right], \tag{2}$$

where $t$ is time, $\hat{Y}_m$ is the discrete Fourier transform (DFT) of the series $y_n = y[(n-1)\Delta t]$ for $n = 1, 2, 3, \ldots, N$, $\Delta t$ is the sampling interval, $s$ is the wavelet scale (scale dilation parameter), $f_m = (m-1)(N\Delta t)^{-1}$ is the Fourier frequency, $N$ is the total number of samples, and $\Psi^*(sf_m)$ is the (theoretical) FT of the complex conjugate corresponding to the wavelet function $\psi$. For the DOG2 mother wavelet,

$$\Psi^*(sf_m) = s^{5/2}\left[\frac{2\pi(m-1)}{N\Delta t}\right]^2 \times \sqrt{\frac{2\pi}{\Gamma(5/2)}} \exp\left\{-\frac{1}{2}\left[\frac{2\pi s(m-1)}{N\Delta t}\right]^2\right\}, \tag{3}$$

where $\Gamma$ is the gamma function. For this particular mother wavelet, the scale is related to the Fourier frequency by the expression $s = s_m = 5^{1/2}2^{-3/2}(\pi f_m)^{-1}$ for $m = 1, 2, 3, \ldots, N$, and the scale domain can be discretized using $s_j = 5^{1/2}2^{-1/2+j\gamma}\pi^{-1}$ for $j = 0, 1, 2, \ldots, J$, where $J = \gamma^{-1}\log_2(2^{-1}N)$. Here, $\gamma$ is a positive constant chosen according to the desired analysis resolution (usually, $\gamma \leq 0.5$).

Because of the redundancy of the CWT coefficients (Farge 1992), the original time series can be reconstructed using a wavelet function other than the analyzing wavelet. The wavelet function used for reconstruction is known as the synthesizing function. If a Dirac delta function is chosen for convenience, the time series can be recovered using the expression

$$y_n = \sqrt{\Gamma(5/2)}\frac{\gamma}{\mu\Delta t^{1/2}} \sum_{j=1}^{J} \frac{\mathrm{Re}[|\tilde{Y}_n(s_j)|^2]}{s_j^{1/2}}, \tag{4}$$

where $\mu = 3.541$ (Torrence and Compo 1998). Analogously to bandpass filtering, certain unwanted features can be removed from the time series if only selected frequencies are included in its reconstruction. This concept is sometimes referred to as ''denoising,'' and it is widely used in several fields.

## 2. Datasets

The radar measurements (Doppler spectra) used in this study were obtained with the ocean surface current radar (OSCR) of the University of Miami working in HF mode (25.4 MHz). It should be stressed, however, that the results and conclusions discussed in later sections are valid for other phased-array HF radar systems. OSCR is a shore-based phased-array antennae system that was typically deployed by using two synchronized control stations (master and slave), located from 20 to 30 km apart, that alternated the emission–reception cycle of the radar waveforms. Each station made independent measurements for nearly 5 min, and the collected data

were processed for 10 min to complete a 20-min sampling cycle. The system was able to cover areas extending up to about 45 km offshore (for current sampling) with a spatial resolution of 1 km and a typical azimuth resolution of 7°. Data were collected from up to 700 preselected locations (grid points), which were usually set with an orthogonal (uniform) spacing of 1 km.

*Experimental venues*

Doppler spectra were collected at three locations corresponding to different experiments: the Shoaling Waves Experiment (SHOWEX), the third phase of the Chesapeake Outflow Plume Experiment (COPE3), and the DUCK94 experiment. The three measuring campaigns were conducted on the U.S. East Coast and they covered coastal areas between North Carolina and Virginia, south of Chesapeake Bay (37°N). The experiments were conducted on different years (within a 5-yr period) and with different purposes, but they covered roughly the same season (early fall). The radar sampling domain for SHOWEX and the DUCK94 experiment encompassed a similar part of the coastal area (about 88% overlap). The distance between these two domains and the COPE3 site was about 70 km. The radar configurations at COPE3 and the DUCK94 experiment were designed to acquire mainly surface current data, whereas the radar configuration at SHOWEX was enhanced (pulse length was doubled from 6.667 $\mu$s) to acquire directional wave information in addition to surface current data (Wyatt et al. 2005).

1) SHOALING WAVES EXPERIMENT (SHOWEX)

SHOWEX was conducted in the coastal area offshore Duck, North Carolina, from early September to late December 1999. It was part of a comprehensive Office of Naval Research initiative to improve the understanding of the properties and evolution of surface gravity waves as they propagate into shallow water. Diverse measuring instruments were used to acquire data, including HF radar, waverider and Air–Sea Interaction Spar (ASIS) buoys, ADCPs, and pressure gauges. Temporary coverage was provided by aircraft and ship expeditions. The detailed experimental configuration, including the instruments relevant for this discussion, is presented in Fig. 1.

The water depth within the area of coverage of the radar system varies from −8.53 to −33.48 m, and it is approximately parallel to the coastline in shallow water (up to about −15 m). In deeper water, the bottom topography becomes irregular because of the presence of several underwater ridges and valleys with height variations on the order of 5 to 10 m that affect the current and wave fields moving through the area. The effect of those bathymetric features on wave propagation will be discussed later and the reader is referred to Cook and Shay (2002) for a discussion of the effects of those features in the current fields (using data from the DUCK94 experiment).

OSCR was used to sample the ocean surface encompassing an area that extended up to 42.3 km offshore (east–west direction) and up to 28 km alongshore (north–south direction). The control stations were located at 36.18°N, 75.75°W (master) and 36.39°N, 75.83°W (slave). Doppler spectra were acquired simultaneously at all points of the sampling grid (marked as dots in Fig. 1) from 1440 UTC 3 November (yearday 307.61) to 2340 UTC 14 December (yearday 348.99) at one-hour sampling intervals (mostly).

Five buoy stations were installed within the coverage area of the radar system during the period of the experiment. The ASIS buoys Bravo and Yankee were located 10.2 and 33.7 km away from the radar master station, respectively. Station Bravo acquired data from 1245 UTC 29 October (yearday 302.53) to 1652 UTC 26 November (yearday 330.70), but the validity of the measurements after 1200 UTC 23 November (yearday 327.5) is doubtful and the corresponding data were excluded from the analysis. Station Yankee measured data from 1210 UTC 30 October (yearday 303.51) to 1056 UTC 13 December (yearday 347.46). Standard oceanographic parameters as well as directional wave spectra were collected at both stations every 20 min. A third ASIS buoy, station Romeo, was located outside the OSCR measuring domain at 54.5 km from the radar master station.

The three directional waverider buoys X1, X2, and X3 were located 6.5, 13.4, and 22.2 km away from the radar master station, respectively, and sampled the ocean surface every 30 min. Station X1 acquired data from 0519 UTC 20 November (yearday 324.22) to 1519 UTC 13 December (yearday 347.64), and station X2 acquired data from 0530 UTC 20 November (yearday 324.23) to 2130 UTC 12 December (yearday 346.9) but there was a period of 10 days where data were not recorded at this site. Station X3 acquired data from 0516 UTC 20 November (yearday 324.22) to 1317 UTC 13 December (yearday 347.55).

2) CHESAPEAKE OUTFLOW PLUME EXPERIMENT (COPE3)

COPE3 was carried out offshore Virginia at the southern side of Chesapeake Bay from mid-October to late November 1997. The experiment was part of a series of Naval Research Laboratory (NRL) sponsored experiments aimed at improving the understanding of the variability of the estuarine plume flowing out of Chesapeake Bay and into the continental shelf. OSCR was deployed to cover the outflow plume (in addition to

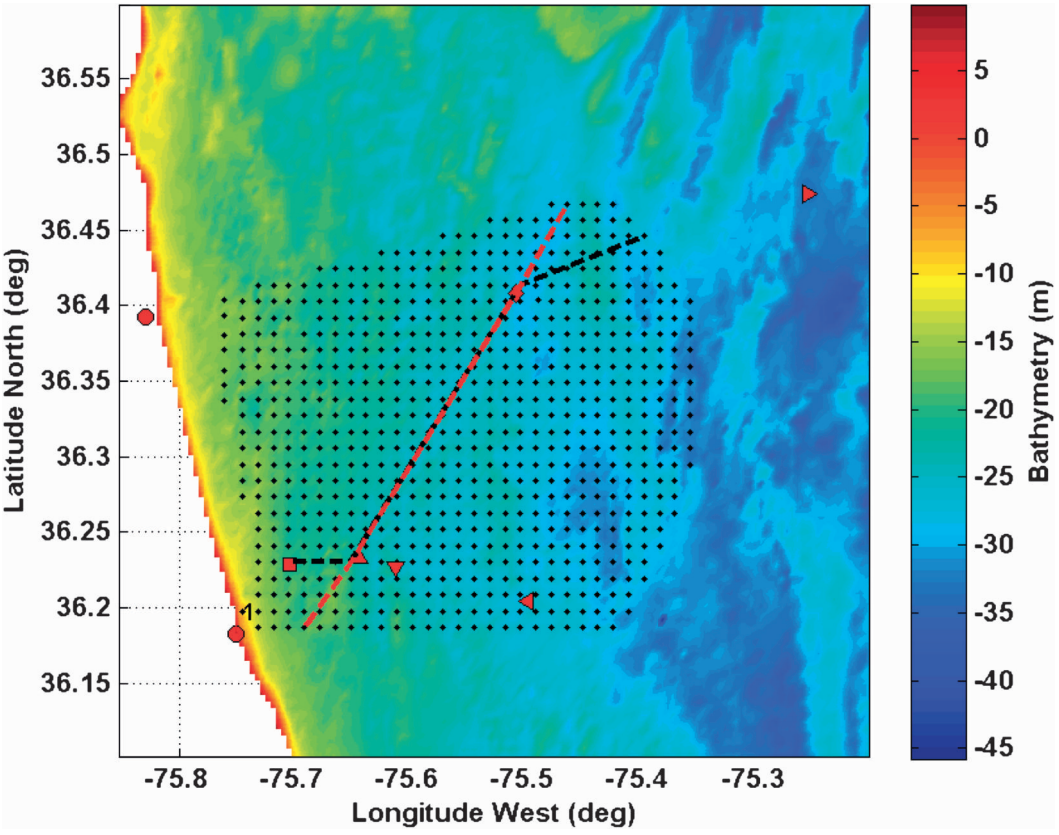


FIG. 1. SHOWEX configuration. Dots indicate the location of OSCR measuring grid points, and the circle markers indicate the locations of its control stations (master to the south). The upward triangle, diamond, and rightward triangle markers represent the locations of ASIS buoy stations Bravo, Yankee, and Romeo, respectively. The square, downward triangle, and leftward triangle markers indicate the locations of waverider stations X1, X2, and X3, respectively. Dashed lines indicate transects selected to investigate wave attenuation (black) and wave growth (red). The color base shows variations in bathymetry (m).

other radar systems and ADCPs). The National Data Buoy Center (NDBC) Coastal-Marine Automated Network (C-MAN) Chesapeake Bay Lighthouse Tower station (CHLV2) was within the sampling domain (Fig. 2). A detailed description of the experiment (and the surface current structure) can be found at Shay et al. (2001a,b).

The bathymetry within the area of coverage of the radar system varies in depth from −7.08 to −24.15 m, and it is characterized by the presence of several underwater ridges and valleys. However, the most prominent feature is the presence of a narrow shipping channel (output from the bay) that enters the area of study from the northwest to the southeast. Local shelf dynamics favor the formation of a mild sloping bottom to the south of the channel and the formation of an ebb-tidal shoal to the north.

OSCR was used to sample the ocean surface covering an area that extended up to 34.04 km offshore and up to 29 km alongshore. The slave radar control station was located at 36.92°N, 75.99°W, and the master station was located at 36.76°N, 75.94°W. Doppler spectra were acquired simultaneously at all sampling points at 20-min intervals from 0110 UTC 14 October (yearday 287.05) to 1050 UTC 30 November (yearday 334.45).

Station CHLV2 consists of a data acquisition and control telemetry (DACT) wave analyzer installed on an offshore platform, and it is located at 36.90°N, 75.71°W in about 15-m water depth (~26 km away from the master station). During the experiment, standard meteorological and oceanographic data along with nondirectional wave spectra were acquired mostly every hour. However, some extended sampling gaps were observed, especially for $H_s$ values larger than 3.4 m. The missing samples accounted for approximately 30% of the total amount of data attainable during the period of interest.

### 3) DUCK94 EXPERIMENT

The DUCK94 experiment was conducted offshore of Duck, North Carolina, from late September to late

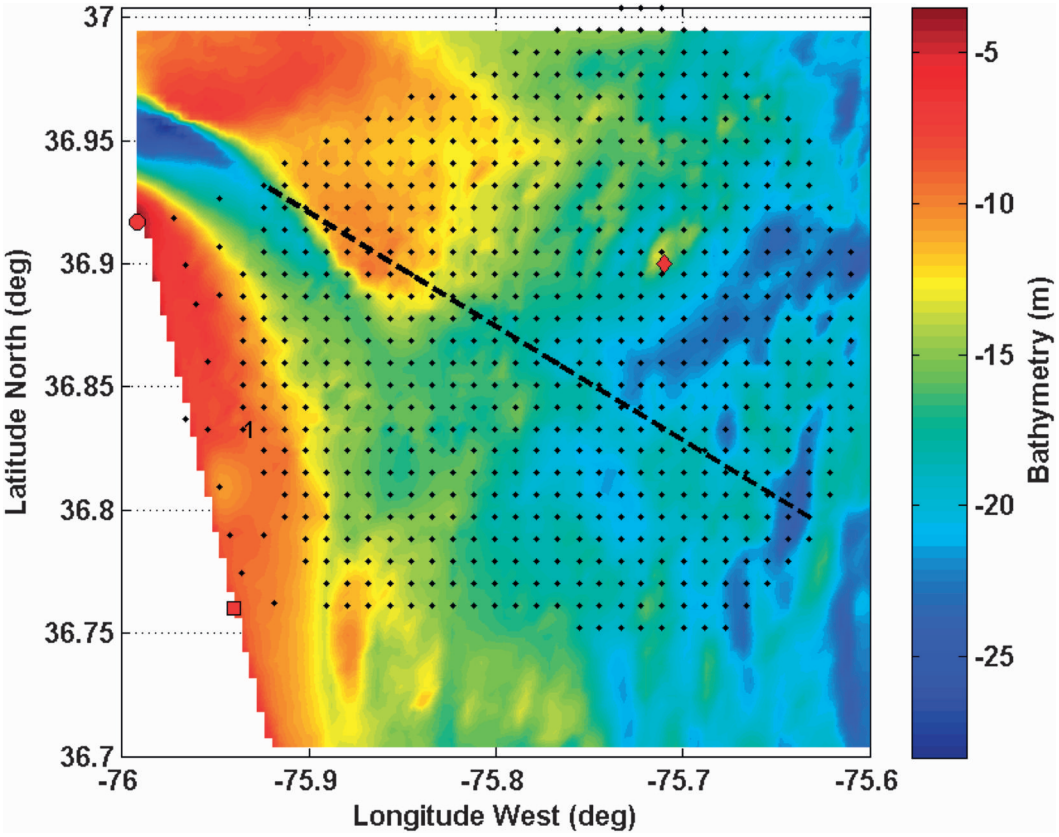


FIG. 2. COPE3 configuration. Dots indicate the location of OSCR measuring grid points, and the square and circle markers indicate the locations of its control stations (master to the south). The diamond represents the location of the NDBC C-MAN station CHLV2. The dashed line indicates transect selected to investigate wave–current interaction. The color base shows variations in bathymetry (m).

October 1994. The multiagency experiment was supported by several institutions [U.S. Army Corps of Engineers, Office of Naval Research (ONR), U.S. Geological Survey (USGS), and NRL] and was aimed to study the structure of the currents over the continental shelf. The experiment included OSCR, bottom-mounted pressure sensors, and high-resolution current meters (vector-measuring current meters). Additionally, NDBC station 44006 was within the radar sampling domain. More details on the experimental setting and the current structure are given in Shay et al. (1998), Cook and Shay (2002), and Haus et al. (2003).

In this experiment, the area of coverage for OSCR extended up to 40.32 km offshore and 25 km alongshore, and the grid was set with an orthogonal spacing of 2 km in the outer (deeper) portion of the sampling domain (Fig. 3). The control stations were located at 36.18°N, 75.75°W (master) and 36.39°N, 75.83°W (slave). Doppler spectra were acquired simultaneously at all grid points with a 20-min sampling interval from 0820 UTC 29 September (yearday 272.35) to 1540 UTC 30 October (yearday 303.65). NDBC station 44006 (General Service Buoy Payload) was located at 36.27°N, 75.50°W in about 25-m water depth and collected standard meteorological and oceanographic data every hour.

## 3. Radar-derived significant wave height observations

An algorithm based on Eq. (1, $\alpha = 1$) was applied to the recorded Doppler spectra to generate time series of $H_s$ observations at every grid point. The estimates were obtained by integrating only over the most energetic side of the Doppler spectrum and by considering only the power above the noise floor level. The latter was computed as the mean value of the power measured at the edge of the corresponding side of the spectrum (0.18-Hz outer frequency band). Only records from the master station were used for the computations, because their quality in all experiments was consistently better than the quality of the slave station records. The raw series obtained were then treated to eliminate defective data

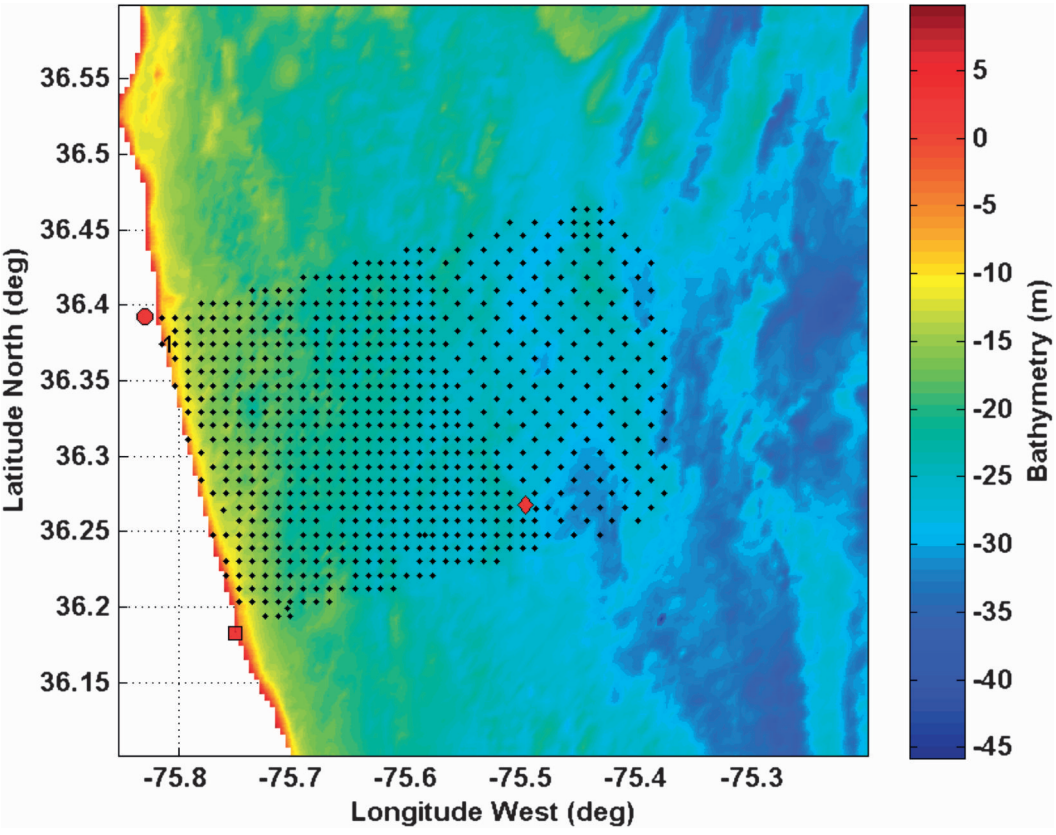


FIG. 3. DUCK94 experiment configuration. Dots indicate the location of OSCR measuring grid points, and the square and circle markers indicate the locations of its control stations (master to the south). The diamond marker represents the location of NDBC station 44006. The color base shows variations in bathymetry (m).

(outliers). Outliers were defined with respect to neighboring data points. Each point in the series was tested against statistics computed from the four closest measurements in time (two ahead and two behind) and data points whose value exceeded three standard deviations measured from the mean value were discarded.

It was observed that the number of outliers increases with range $r$ as the signal-to-noise ratio (SNR) decreases (Table 1), but its value was not significant at low ranges ($r < 15$ km) in any experiment. Defective data were replaced by linearly interpolated estimates, but time series segments with large gaps of missing data (more than 12 consecutive samples) were not considered for subsequent analysis.

### *a. Assessment of the correction factor (bias of methodology)*

The quality of data from the DUCK94 experiment was significantly better than that of the other experiments (Table 1) and was therefore chosen to determine the correction factor $\alpha$ in Eq. (1). Because no clear directional tendencies were identified from the analysis of the datasets, the value of $\alpha$ was computed simply as the ratio of mean radar-derived to buoy-measured $H_s$ at the location of NDBC station 44006. The final result yielded $\alpha = 0.5819$. It should be noted that, although the expression was expected to provide a better fit for the range $H_{\text{rms}} \geq 0.3/k_o$ ($H_s \geq 2.26$ m; Barrick 1977a), consideration of values outside this constraint did not change $\alpha$ significantly. Also, the apparent directional insensitivity confirms that the dependence of Eq. (1) on the radar-look angle is weak compared to other sources of variability.

A comparison between radar-derived and buoy-measured estimates is presented in Fig. 4. It is observed that the spread of $H_s$ is uniform along the entire range of values. It is also apparent that there is a well-defined linear fit between both datasets once the correction factor has been introduced. This feature further validates the assumption of linear proportionality for $H_s$ (correction factor $\alpha$) in Eq. (1). The RMS difference and the correlation coefficient between estimates were found to be 0.31 m and 0.95, respectively (9% mean relative error). Results from the application of Eq. (1),

TABLE 1. Amount of deficient data recorded by the radar at each experiment site.

| Expt | Sampling interval | Range (km) | Percent of samples | | |
|---|---|---|---|---|---|
| | | | Missing | Defective | Tot |
| SHOWEX | 1 h | 6.5* | 1.9 | 6.7 | 8.6 |
| | | 10.2* | 1.9 | 6.3 | 8.2 |
| | | 13.4* | 1.9 | 6.9 | 8.8 |
| | | 22.2* | 1.9 | 9.0 | 10.9 |
| | | 33.7* | 1.9 | 18.3 | 20.2 |
| COPE3 | 20 min | 6.6 | 5.6 | 7.4 | 13.0 |
| | | 10.2 | 5.6 | 7.5 | 13.1 |
| | | 26.0* | 5.6 | 12.3 | 17.9 |
| | | 33.8 | 5.6 | 30.3 | 35.9 |
| DUCK94 | 20 min | 24.6* | 0.2 | 1 | 1.2 |

* Location is nearby a buoy station.

as shown in Fig. 4, differ from other directional methodologies that tend to overestimate $H_s$ for higher sea states and in which the spread tends to increase with $H_s$ (Wyatt et al. 1999; Wyatt 2000).

### b. Validation of the methodology and effective range

The correction factor obtained before was used in Eq. (1) to estimate $H_s$ from Doppler spectra collected during COPE3 and SHOWEX. The derived observations were then compared to the gauge/buoy measurements acquired at stations CHLV2, Bravo, Yankee, X1, X2, and X3. The results are shown in Fig. 5 and summarized in Table 2. It is apparent that, for short ranges, the radar-derived $H_s$ values are in good agreement with in situ measurements and provide as good a fit as the calibration case (DUCK94 experiment). However, the quality of the radar-derived $H_s$ values degrades as the range increases. The correlation coefficient decreases from 0.96 at station X1 (6.5 km range) to 0.68 at station Yankee (33.7 km range), and the RMS difference increases consistently in the comparisons to both the ASIS and waverider buoys.

The increasing RMS difference between the radar-derived estimates and the gauge/buoy measurements with range is related to the ability to distinguish between signal and noise from the recorded backscattered power. Figure 6 presents the variation in range of the peak in the second-order backscatter region of Doppler spectra and the corresponding noise floor. It is observed that, as the range increases, the peak of the second-order backscatter region becomes closer to the noise floor, and therefore the associated second-order structure becomes increasingly masked. Similarly, the noise floor (as computed here) decreases with increasing range until it reaches a minimum value of about −189 dB, but it becomes modulated, increasing during the daytime

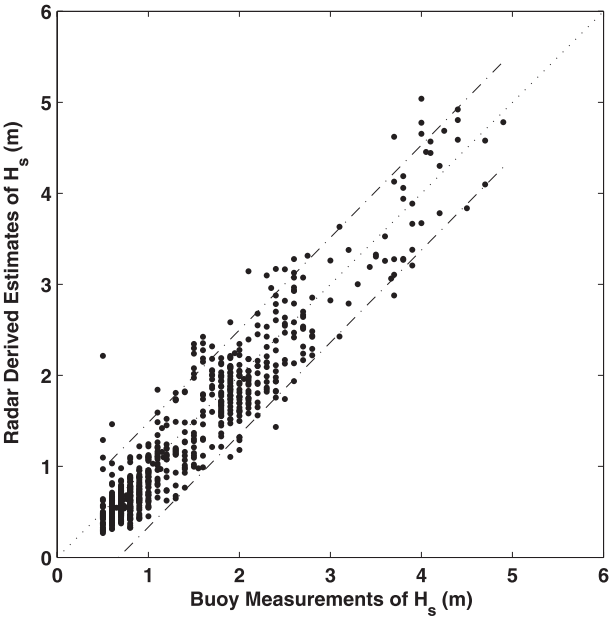


FIG. 4. Comparison of significant wave height estimates from OSCR (correction factor $\alpha$ applied) vs buoy measurements acquired during the DUCK94 experiment. Dashed–dotted lines correspond to the 95% confidence interval.

because of RFI in the site (presumably). At short ranges (smaller than ~10.2 km; e.g., stations Bravo and X1 in Fig. 6), the noise floor is significantly higher than the RFI level but the backscatter power is very strong. The average SNR from the second-order peak to the noise floor [$SNR_{(2)}$] is higher than about 22 dB and in very few cases takes values smaller than 15 dB. This portion of the radar sampling provides for the best estimates from Barrick's model. At longer ranges (~13.4 km; e.g., station X2 in Fig. 6), the value of the noise floor is just above the RFI level and the backscatter power is still strong. The average $SNR_{(2)}$ is approximately 17 dB and only in very few cases falls below 10 dB. The quality of the estimates in this portion of the radar sampling area was found to be good (when no major temporal electromagnetic signals from extraneous sources were observed). At intermediate ranges (~22.2 km; e.g., station X3 in Fig. 6) the noise floor has reached the RFI level, but the return signal is strong enough to keep the average $SNR_{(2)}$ at about 11 dB in the entire interval. Under such conditions, the estimates become more scattered and their quality becomes dubious, especially during the daytime. Finally, at long ranges (~33.7 km; e.g., station Yankee in Fig. 6), the second-order backscatter power is weak and so close to the RFI level that the average $SNR_{(2)}$ is only about 5 dB. The variations in noise floor mask the return signal in the second-order region and lead to erroneous estimates of the second-order backscatter power

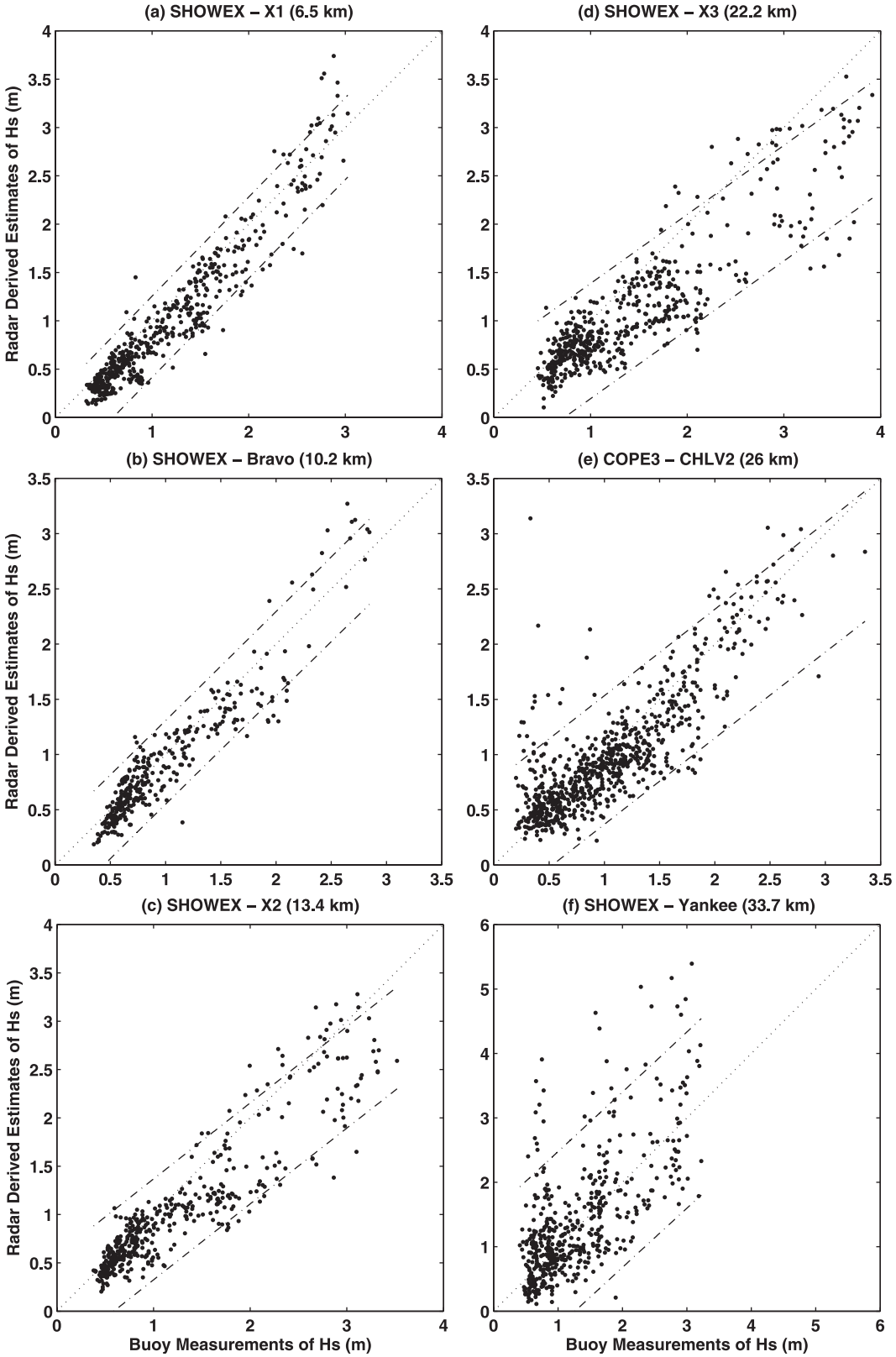


FIG. 5. Comparison of significant wave height estimates from OSCR vs gauge/buoy measurements acquired during COPE3 and SHOWEX. Dashed–dotted lines correspond to the 95% confidence interval.

TABLE 2. Spread and fitting parameters for intercomparisons between radar-derived and in situ observations of $H_s$.

| Expt | Buoy/device | Range (km) | $\rho$[a] | Error | | | $m$[c] | $b$[d] | $n$[e] |
|---|---|---|---|---|---|---|---|---|---|
| | | | | Mean (m) | REL (%)[b] | RMS (m) | | | |
| DUCK94 | 44006 | 24.6 | 0.95 | −0.09 | −8.5 | 0.31 | 1.02 | −0.11 | 742 |
| COPE3 | CHLV2 | 26.0 | 0.83 | −0.05 | 6.1 | 0.33 | 0.78 | 0.17 | 761 |
| SHOWEX | X1 | 6.5 | 0.96 | −0.16 | −18.9 | 0.27 | 1.03 | −0.19 | 513 |
| SHOWEX | Bravo | 10.2 | 0.94 | −0.07 | −8.4 | 0.21 | 0.98 | −0.06 | 325 |
| SHOWEX | X2 | 13.4 | 0.92 | −0.21 | −14.2 | 0.37 | 0.79 | 0.06 | 445 |
| SHOWEX | X3 | 22.2 | 0.89 | −0.33 | −21.8 | 0.50 | 0.71 | 0.08 | 513 |
| SHOWEX | Yankee | 33.7 | 0.68 | 0.09 | 13.6 | 0.70 | 0.92 | 0.19 | 513 |

[a] Correlation coefficient.
[b] Relative error.
[c] Slope of best linear fit to the data (least squares sense).
[d] Intercept of best linear fit to the data (least squares sense).
[e] Number of common data points.

[integral in Eq. (1)] that are strongly correlated to the diurnal cycle, distorting several consecutive samples for long periods of time. If the sea state does not change significantly during those periods, then the distorted values are associated with similar values of buoy-measured $H_s$ and cause the grouping effect shown in Fig. 5f.

The tendencies discussed apply to any experimental setting, but actual ranges and power levels can change. In any case, it is clear that the limit of good quality estimates at a particular site might be set conservatively to the range where the noise floor reaches the RFI level during the daytime. Based on this premise, the values of maximum effective range were estimated to be 14.5 km for SHOWEX, 12.8 km for COPE3, and 14.8 km for the DUCK94 experiment. The effective range, however, is expected to extend significantly seaward during the nighttime and in cases where $\mathrm{SNR}_{(2)}$ at the limit is greater than 11 dB.

An additional contribution to the variability observed in Fig. 5 comes from the presence of abnormal spatial patterns of backscatter power. These events were characterized by increased radar return and by the presence of additional prominent peaks within the second-order backscatter power region of Doppler spectra. They were found to be mostly associated to the interaction of strong currents with antennae side lobes (Wyatt et al. 2005) and to directional radio interference. The occurrence of these events was evident in the estimates of noise floor and the net effect was the overestimation of $H_s$. Such occurrences were observed in both COPE3 and SHOWEX and were associated with the presence of radial sectors of increased noise floor levels in the radar domain. Their spatial distribution in a typical case is shown in Fig. 7. In some intervals (particularly during SHOWEX), these abnormal patterns appeared for long periods of time (lasting several consecutive or nearly consecutive sampling intervals) and their effect was extended further in the time series by the filtering applied to the $H_s$ observations. However, it is evident that the effect of such patterns in observations obtained at small ranges was limited.

It should be mentioned that restrictions in the storage capacity of OSCR also introduced errors in the estimates. Doppler spectra ordinates in this system were stored as unsigned 2-byte integers and the dynamic range was therefore limited to 48.16 dB. At short ranges, this value was exceeded on occasion by the SNR recorded by the master station (in all the experiments) and thus induced erroneous estimates of noise floor as its value fell below the minimum storage value. This hardware limitation, however, had little impact on the results presented in this work, because the grid points used for the various analyses were confirmed to be within the system allowable storage range.

### c. *Wavelet-based filtering of radar-derived observations*

The radar-derived $H_s$ values were further filtered to reduce their scatter and to eliminate the contribution of the unrealistic features already discussed. The main components of every time series were identified by using Eq. (2). In each case, the scale domain was first discretized into 29 components ($\gamma = 0.25$) following a logarithmic (base 2) increment that varied from 0.50 to 64.42 (equivalent to a variation in period $T$ ranging from 2 h to 10.67 days). Then, each series was reconstructed, including only scales in the range $s \geq 3.39$ ($T \geq 13.45$ h). This limit was selected because it resulted in the smallest RMS error when comparing the reconstructed series to the buoy recordings. The minimum equivalent period in the range is also associated to the interval (cone) of influence of a feature lasting approximately 8 h and corresponds to the maximum observed interval of abnormal consecutive samples. The DUCK94 and SHOWEX series

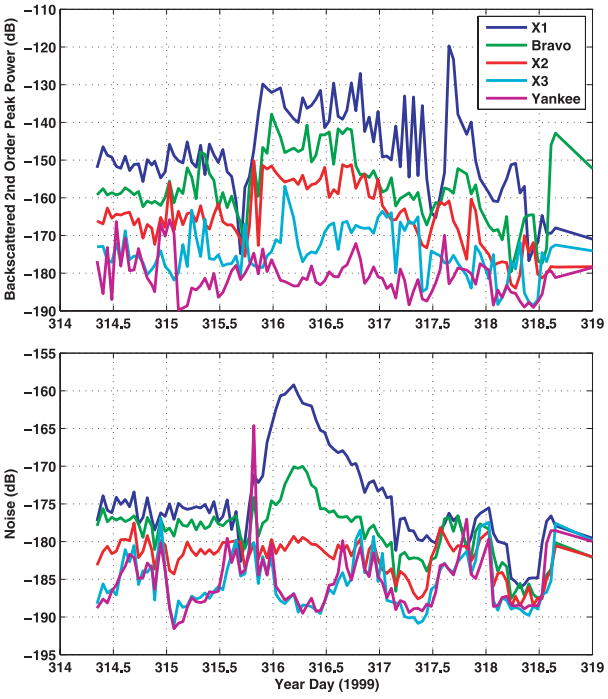


FIG. 6. Time variations of (top) the second-order peak backscattered signal and (bottom) the corresponding noise floor for locations near buoy stations in SHOWEX.

were not filtered (explicitly) for tidal components because those were found to have a negligible impact in the total measured energy in the presence of storm events (Cook and Shay 2002). The COPE3 series were not filtered because the tidal components near the mouth of Chesapeake Bay were of interest to study the wave propagation in the region (section 4c).

Analysis of the data showed that the wavelet filtering is consistent with other techniques (e.g., Fourier bandpass filtering) in the sense that the discarded scales minimize the contribution of features with corresponding equivalent frequencies. As the smaller scales are increasingly discarded, higher-frequency features in the time series are less apparent. However, results from the buoy time series showed that components with periods smaller than 13.45 h ($s \leq 3.39$) were rare and contributed only about 0.1% of the total energy contained in the record. Some local features [e.g., the double peak shown in Fig. 11 (dot markers), which corresponds to a period of about 6 h] would be significantly diminished once the filtered series excludes frequencies in the range $s < 1.69$ ($T < 6.7$ h), but its time domain signature would be fully removed until both peaks combine into a wider peak for $s < 2.39$ ($T < 9.6$ h).

The effect of the neglected components on the accuracy of the filtering technique can be observed in Fig. 8, where the error in the estimates corresponding to a storm recorded during SHOWEX is shown. It is noticed that discarding scales (solid line) in the range $s < 3.39$ (i.e., including 62% of the components in the reconstruction) introduces an RMS error of 0.15 m with respect to the original (unfiltered radar-derived) series. When the error is computed with respect to the unfiltered buoy measurements (dashed–dotted line), the energy contribution of the components included in the reconstruction corresponds to the best estimate of the energy content of the wave field. In this case, the neglected components account for about 5% of the total wave energy measured by the radar at the peak of the event (see Fig. 9). It can also be observed, from Fig. 8 and from the expression for equivalent Fourier frequency in Eq. (3), that consideration of additional scales for reconstruction would only imply a slight increase in RMS error, but it would result in a significant decrease in the equivalent Fourier period for the included components. For example, inclusion of scales in the range $s > 1$ (i.e., considering 86% of the total number of scales) would result in an RMS error increase of 4 cm (when compared to results from the range $s > 3.39$) and would be equivalent to incorporate components with periods larger than 4 h in the smoothed series. A similar tendency was observed when the RMS difference was computed with respect to the filtered buoy-measured series (dotted line in Fig. 8). The error distribution in this case does not deviate significantly from the unfiltered buoy-measured curve once the number of components exceeds 60%.

From the previous discussion and given the estimated RMS errors at the peak of the storm (Fig. 9), it can be concluded that the smoothing of the time series is not very sensitive to changes in scale (or equivalent period) once an optimum value has been reached. Because the tendencies observed in the error distribution displayed in Fig. 8 are consistent with results obtained from the analysis of other segments of the data series (different storm systems) and with results from the analysis of the entire record, the use of the selected scale range was further validated.

It should be noted that the inclusion of all the components in the reconstruction does not fully recover the original time series. This error is associated with the characteristics of the record in conjunction with its numerical treatment (selected mother wavelet, CWT computation, synthesizing function, etc.) and does not change significantly if the resolution (i.e., the number of components in the characterization) is increased. In fact, the gain in accuracy for full reconstruction remains marginal once the number of components exceeds 8 [$\gamma = 1$ in Eq. (4)].

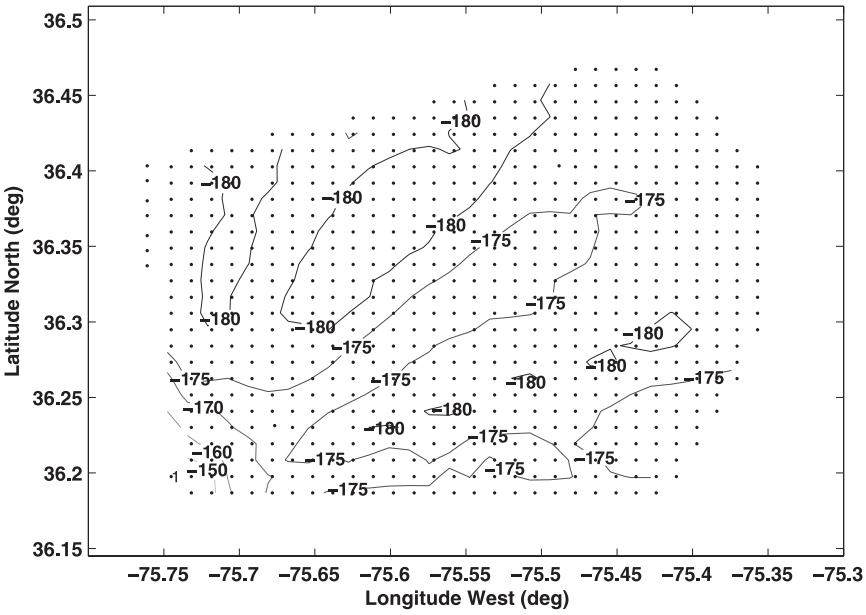


FIG. 7. Distribution (abnormal) of noise floor (dB) estimated from Doppler spectra measured at 1540 UTC 01 Dec 1999 during SHOWEX.

## 4. Energy evolution in coastal areas

Once the time series of radar-derived $H_s$ were filtered, selected segments were compared to buoy measurements and to theoretical results from wave propagation models. Distinctive storm conditions along selected wave propagation paths were chosen, and the accuracy of the filtering scheme (and the overall treatment of the data) was assessed. The results are presented next.

### *a. Wave energy attenuation*

The special case of wave energy attenuation resulting from the interaction of the wave field with the sea bottom

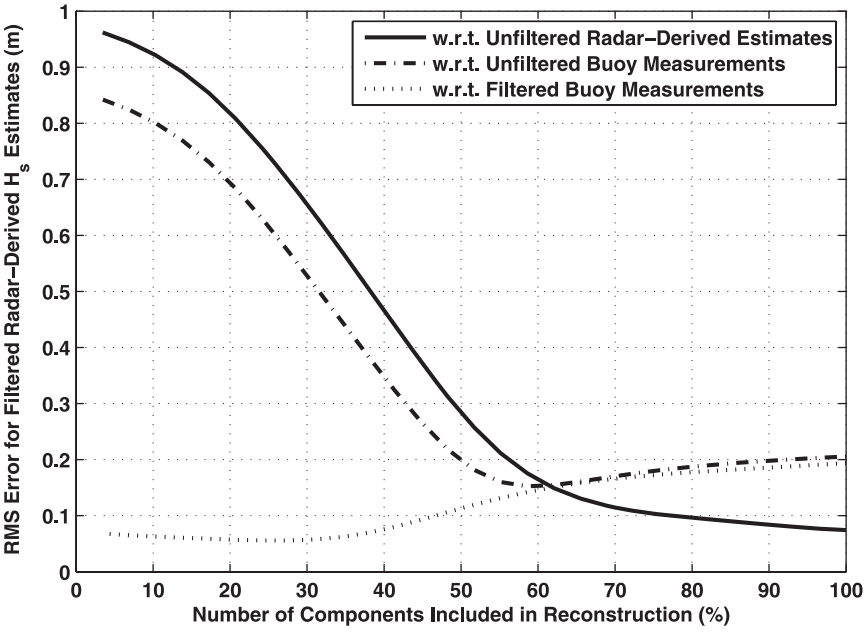


FIG. 8. Error in the filtering procedure as a function of the number of components included in wavelet reconstruction (low scales neglected). The data analyzed correspond to a storm event recorded at station Bravo between yeardays 315.5 and 317.5 during SHOWEX.

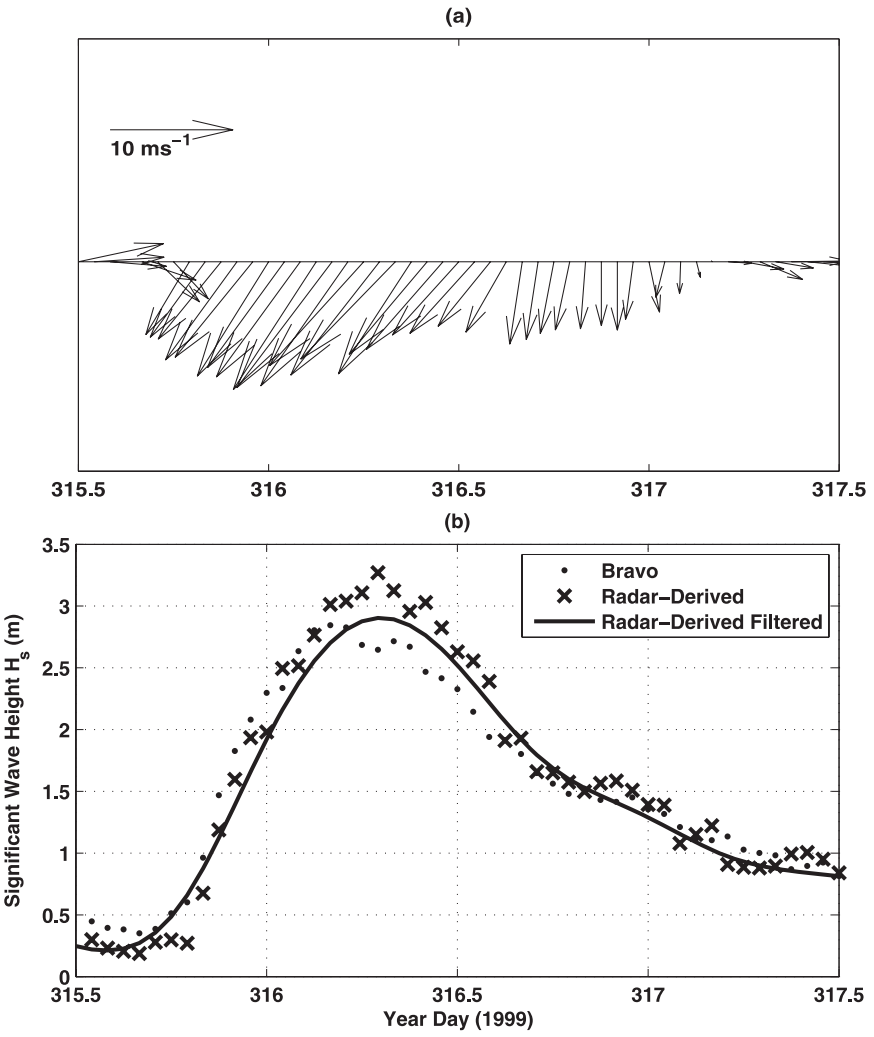


FIG. 9. (a) Wind and (b) wave characteristics of a storm event measured at stations NDBC 44014 and Bravo. Arrows in (a) indicate direction where the wind is blowing toward (wind speed shown at instrument level).

was studied using data from SHOWEX; in particular, data from a storm that occurred between yeardays 315.5 and 317.5 were used (Fig. 9). The event developed after a transitional period of about 10 h during which the wind speed decreased and changed direction clockwise from south-southwest to north-northeast. Following that transition, the wind direction remained fairly constant varying between 30° and 35° azimuth (meteorological convention), providing unlimited fetch, and the wind speed increased gradually from 3.4 (yearday 315.75) to 13.5 m $s^{-1}$ at the peak of the storm (yearday 316.17). The development of the wave field followed closely the wind input (Fig. 9b), increasing in $H_s$ from 0.35 m at the end of the transition period to 2.85 m at the peak of the storm.

Radar-derived $H_s$ observations and theoretical $H_s$ estimates were obtained at the peak of the storm along the transect (black dashed line) shown in Fig. 1. This cross-shelf transect was chosen to include the most buoy stations while maintaining alignment with the direction of wave propagation. In particular, the segment between stations Yankee and Bravo was aligned at 33° azimuth and therefore corresponded closely to the incidence angle of the wave field. The radar-derived $H_s$ values were obtained directly from the grid points closest to the transect and the theoretical estimates were computed from modified wave spectra obtained by applying a transformation function (Bouws et al. 1985, 1987) to the wave spectrum recorded at station Romeo.

The legitimacy of the theoretical estimates is based on the location of the area of study. The transformation function was derived as part of what it is known as the TMA spectrum and included an extensive database of

wave spectra measured in the coastal area centered at the Coastal Engineering Research Center (CERC) Field Research Facility in Duck, North Carolina, and coincided roughly with the location of the radar sampling domain in SHOWEX. Thus, both radar-derived and theoretical estimates were obtained for similar (if not identical) conditions of wind generation (onshore winds), water depth, and sea bottom materials.

The comparison of radar-derived and theoretical $H_s$ values is shown in Fig. 10. The theoretical $H_s$ values were strongly correlated with variations in bathymetry, which was expected because the transformation function depends directly on water depth. As the wave field propagated shoreward, it experienced an energy decrease of 18% (~0.63 m) between stations Romeo and X1. This tendency of the theoretical $H_s$ was confirmed by the in situ measurements at stations Bravo and X1 (where differences smaller than of 1.5% were found) and by the reference measurement at station Romeo, but a significant deviation was observed at the location of station Yankee (~6% overestimation). This discrepancy is likely to be related to the inability of the theoretical model to represent the transition period in which the wave field adjusts to the increase of water depth once it passes the ridge depicted in Fig. 10b at about 35 km. The effect of this feature, however, was localized and should not affect the model-derived estimates within the effective radar domain ($r < 30$ km).

The filtered and unfiltered radar-derived $H_s$ series are also depicted in Fig. 10. Although the unfiltered $H_s$ values show large scatter and overestimation of the energy level, the filtered radar-derived estimates agree closely with their theoretical counterpart. The corresponding RMS difference was found to be 0.1 m (2% mean relative error). The absolute difference between the filtered radar-derived $H_s$ and the in situ measurements at X1 and Bravo was on the order of 2%.

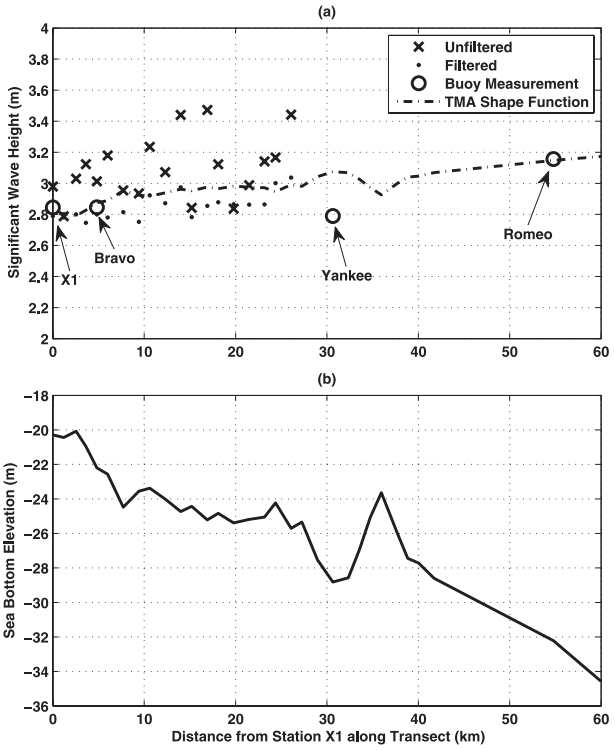


FIG. 10. Comparison of $H_s$ estimates for yearday 316.17 (0400 UTC 12 Nov 1999) along a transect following the wave propagation: (a) radar-derived, model-derived, and available buoy measurements and (b) the corresponding bathymetry.

### b. Wave energy growth

The case of wave energy growth due to the forcing of wind under fetch-limited conditions was also studied with data from SHOWEX, in particular, with data from the storm shown in Fig. 11. The event lasted approximately from yearday 309.54 to yearday 311.21 and followed a period of about 10 h during which the wind was blowing predominantly from the west (270° azimuth). After yearday 309.54, the wind direction switched rapidly to the southwest and the wind speed increased uniformly from 3.4 to 10.4 m $s^{-1}$ at the peak of the event (yearday 310.21). The wind direction remained fairly constant at 210° azimuth for seven hours prior to the occurrence of the peak and then it switched slightly to 227° azimuth. The wave field in this storm showed two well-defined peaks separated by an interval of 6 h (see dotted line in Fig. 11b). The peak at yearday 309.96 was most likely caused by the interaction of early sea propagating to the east with swell propagating to the west. Conversely, the peak at yearday 310.21 was largely induced by the southwest wind field described.

It is apparent from Fig. 11b (cf. Figs. 11b, 9b) that the unfiltered radar-derived estimates for this event are more scattered. The higher variability was expected as the second-order backscattered power is greatly reduced for measurements of small sea states causing its misrepresentation in the integrand of Eq. (1). However, of most significance is the fact that Eq. (1) loses accuracy as the sea state decreases because Barrick's derivations followed the assumption that the peak wavenumber in the wave spectrum is smaller than the radar wavenumber. It is observed that the radar estimates fail to reproduce the peak at yearday 309.96, although that inability was likely associated with oversmoothing and underestimation caused by electromagnetic interference present during the corresponding measurements.

Radar-derived and theoretical $H_s$ values were obtained at the peak of the storm along the transect shown in Fig. 1 (red dashed line). The alignment of this transect

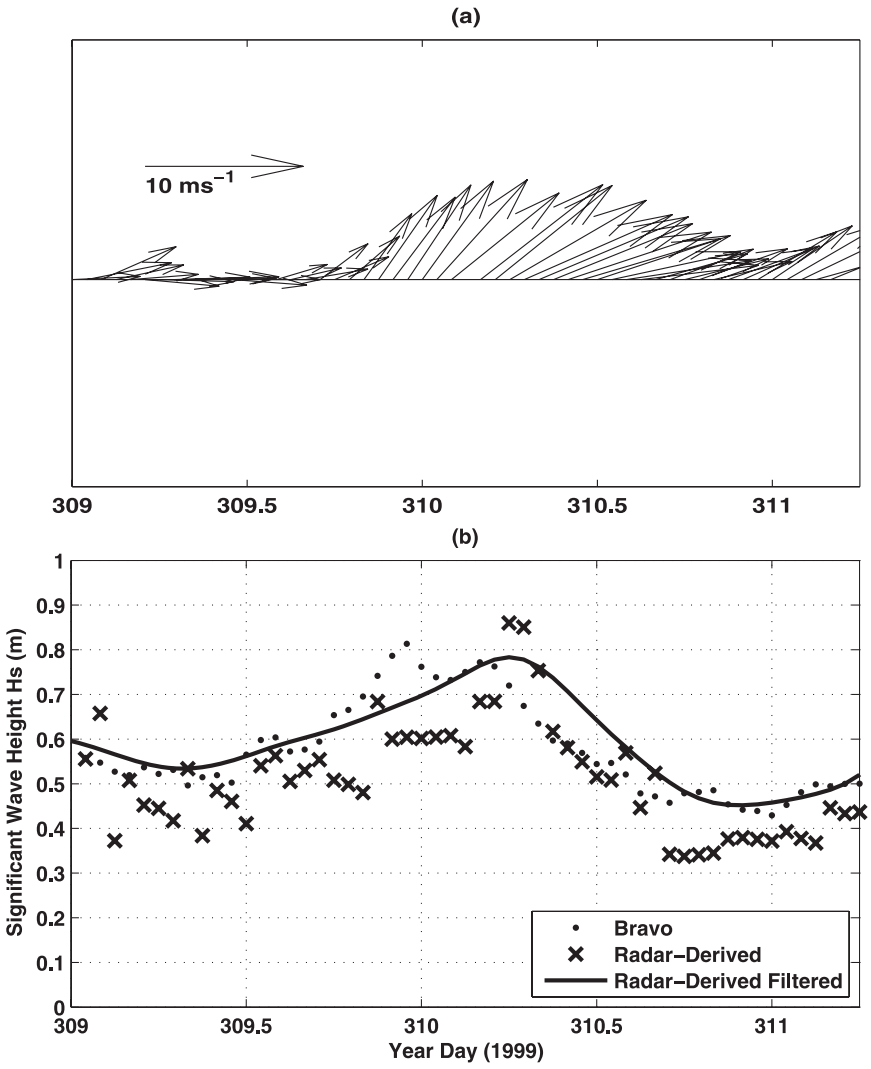


FIG. 11. As in Fig. 9, except for yeardays.

coincided with the dominant wave direction and with the location of stations Bravo and Yankee. The theoretical $H_s$ estimates used for comparison purposes were obtained using the energy growth law developed for the Joint North Sea Wave Project (JONSWAP; Hasselmann et al. 1973), including the concept of effective fetch (Donelan 1987). First, the buoy measurements at stations Bravo and Yankee were used to estimate the $H_s$ corresponding to pure wind–sea by integrating the wave energy spectrum for frequencies greater than 0.16 Hz only (i.e., $f \geq 0.16$ Hz). Then, the energy growth law was fitted to the resulting values at both locations. Finally, the theoretical $H_s$ corresponding to the actual wave field (sea and swell combined) was estimated by adding the contribution of swell (integral of wave spectrum in the range $f < 0.16$ Hz) to the JONSWAP base line. The results of the various phases of this process are shown in Fig. 12. It is observed that, as the wave field propagated from station Bravo to station Yankee, the total amount of energy increased about 41% and the wave spectra measurements showed that the peak spectral frequency decreased from about 0.33 Hz to about 0.26 Hz, which corresponds to a classic case of wave growth. Measurements at station X1 (not shown) confirmed that the tendency observed in the model estimates (solid line) extends farther onshore along the selected transect.

It should be noted that the use of different energy growth laws to estimate the theoretical $H_s$ should not have a significant impact in the results presented here because the corresponding fetch lies within an interval where most growth curves seem to converge (Young 1999). The wind speed found from the JONSWAP fitting

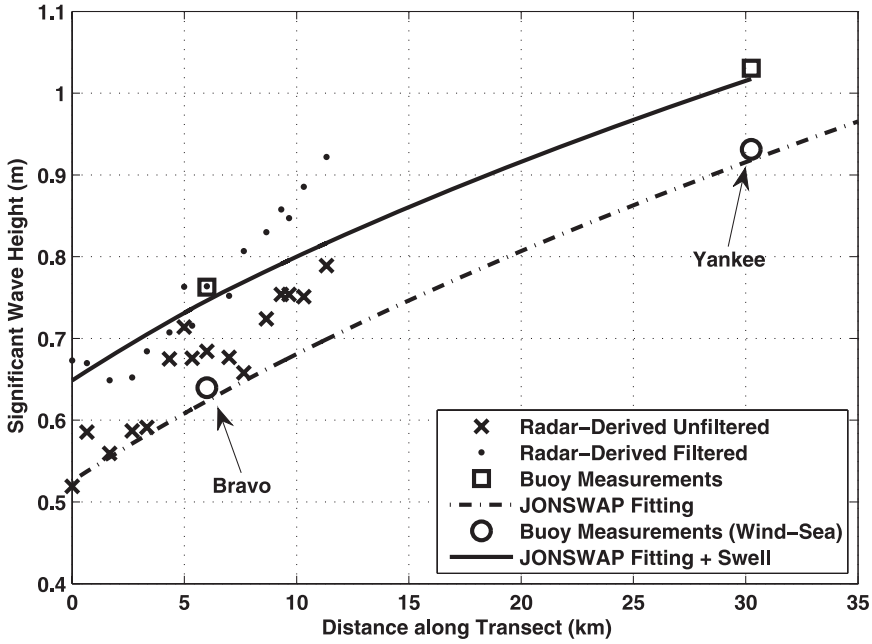


FIG. 12. Comparison of $H_s$ estimates for yearday 310.21 (0500 UTC 06 Nov 1999) along a transect following the wave propagation. Solid line shows theoretical estimates.

agreed closely (within 5% error) with the average value observed during the entire storm event.

The filtered radar-derived $H_s$ values obtained for the grid points considered along the studied transect are also shown in Fig. 12. It is observed by comparing to theoretical $H_s$ that, as in the case of wave energy attenuation studied before, the applied filtering technique seems to reduce the scattering in the data and to provide a more accurate estimate of the energy content of the wave field. However, the radar-derived estimates show a tendency to overestimate the theoretical value as the range increases.

The RMS difference between the radar-derived and model $H_s$ was found to be 0.08 m (10% mean relative error) and 0.05 m (3% mean relative error) for the unfiltered and filtered cases, respectively. Both values are significantly smaller than the ones obtained for the wave attenuation case, but this is not necessarily associated with a better theoretical estimate. The quality of the radar-derived data (theory limitations, scattering conditions, defective and missing samples, etc.) in a particular segment (and location) also plays a significant role in assessing the accurate energy level in any condition of wave propagation. The RMS difference from the filtered radar-derived series corresponds to about 30% of the expected increase of energy in the effective range (see Fig. 12). Therefore, the treated estimates can be used effectively only to investigate the wave growth tendency in the effective radar domain.

### c. *Wave shoaling due to countercurrents*

The case of interaction of a wave field propagating against the flow of a surface current was investigated with data from COPE3. Because many of the findings were previously reported in Haus et al. 2006, this section will focus only on the comparisons of theoretical and radar observations of maximum individual wave height $H_{\max}$ along the propagation path shown in Fig. 2. The event was recorded at yearday 287.78 and occurred during a relaxation period associated with low values of $H_s$ (~0.61 m). The wind was blowing temporarily from the southeast (for about 3 h) at 5.8 m $s^{-1}$ and encountered a current flowing with a maximum core velocity of 1.12 m $s^{-1}$.

The associated wave field (at the location of CHLV2) was dominated by swell with a peak frequency of 0.08 Hz (244-m wavelength) and also had a strong contribution of wind–sea that peaked at 0.17 Hz (54-m wavelength). Thus, the theoretical $H_{\max}$ variations of the peak sea and swell components were estimated independently. The contribution of swell was investigated by using a model of wave propagation (shoaling and refraction) based on wave ray theory (Dean and Dalrymple 1991). Because no wave directional information (directional spectra) was available for the area of study, all incidence directions from the east quadrant were investigated. The results showed that most of the energy associated with the main swell components was likely to be concentrated

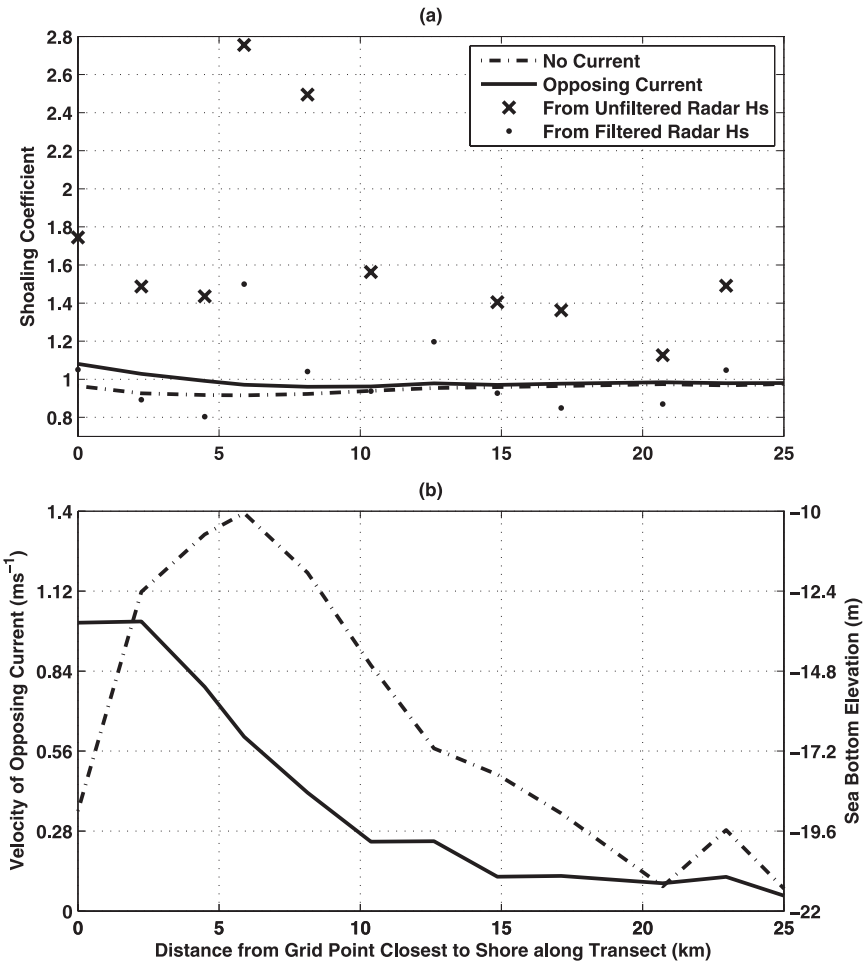


FIG. 13. (a) Theoretical and radar-derived estimates of the variation of shoaling coefficient as a function of water depth and opposing current along a selected transect, and (b) the corresponding variations of water depth (dashed–dotted) and current (solid). The data were measured at yearday 287.78 (1840 UTC 14 Oct 1997) during COPE3.

and dissipated nearby some of the existing bathymetric features, especially at the edges of the shipping channel. On the other hand, the main components of the wind–sea were assumed to propagate against the current following the direction of the wind and were modeled (as linear waves) considering only the effects of shoaling (no refraction).

Because $H_{\max}$ cannot be directly inferred from the radar measurements, $H_s$ was taken as an estimator of its value. This assumption is based on the fact that $H_s$ is defined as the average of the highest one-third of waves in a given wave field and therefore it is proportional to (or at least an indicator of) the highest individual wave in the trend.

Figure 13 presents the comparison of theoretical and radar-derived estimates of $H_{\max}$ in terms of the variation of the shoaling coefficient along the selected transect. The shoaling coefficient was computed by normalizing $H_s$ with respect to a long-range value that was not significantly affected by current or underwater features and therefore includes the contributions of local sea and swell. The dot and cross markers correspond to the filtered and unfiltered radar-derived estimates, respectively. The dashed–dotted line represents the expected wave height variation of the peak sea component resulting from the effect of the bathymetric profile only (Fig. 13b), and the solid line represents the expected variation in wave height when the effects of the countercurrent (Fig. 13b) are included. It is observed that at intermediate distances (5–15 km) the wave field seems to be dominated by refracted swell under breaking or near-breaking conditions. The existing bathymetric feature that peaks at 5.89 km along the transect (about 36.9°N, 75.87°W in Fig. 2) causes a significant concentration of

swell and dissipates a considerable portion of this energy as the wave field propagates farther downwind (~60% loss in $H_{max}$). Such a tendency was confirmed by results from the wave propagation model for swell incidence from the southeast quadrant (Haus et al. 2006). It is also clear from Fig. 13 that at distances smaller than 5 km, where the contribution of wind–sea is expected to dominate, the countercurrent plays a significant role in the observed $H_{max}$ increment. At this range, the increasing current velocity is responsible for the increment of wave height that peaks at the edge of the radar sampling area (where the velocity is larger) and the tendencies in both measurements and theory show agreement. These results are consistent with wave growth tendencies observed in the entire radar domain (Haus et al. 2006).

Although it is apparent that the filtered observations offer a better representation of the behavior predicted by theory, the results should be taken with caution. Most of the difference between both radar-derived series comes from a strong bias introduced by variations of $H_{max}$ at the grid point used for normalization. If that bias is eliminated, then the major contribution to the difference between both series becomes the segment between 10 and 15 km, where the unfiltered estimates predict 25% larger $H_{max}$. Unfortunately, because of the lack of more detailed independent wave measurements, this study could not be pursued further and it was not possible to obtain more conclusive results. Even though a more extensive theoretical approach is required to assess this phenomenon with better accuracy, taking into account the contribution of the many components of the wave field (and the interaction among them), the results show that the HF radar is able to identify the associated wave growth tendencies.

## 5. Summary and conclusions

The accuracy of a phased-array HF radar system to measure $H_s$ was established for different scenarios of wave propagation. First, a technique to calculate $H_s$ from the Doppler spectra records was evaluated. The resulting time series were wavelet filtered and compared to results from independently validated wave propagation models.

The radar provided unbiased observations of $H_s$ with variance (RMS difference) on the order of 0.30 m (9% mean relative error) within the radar effective range for a variety of conditions and locations. The variance of the observations was shown to be independent of the sea state [within the $H_s$ range studied ($H_s < 6$ m)], but it was greatly influenced by variations in the SNR corresponding to the second-order region of the Doppler spectrum. Accordingly, the quality of the estimates decayed as the range increased and the backscatter power approached the noise floor level. The effective range extended to the limit where diurnal variations of RFI dominated the second-order backscatter power.

The filtering technique was able to greatly diminish the contribution of unrealistic features and faulty data inherent to radar sampling. It is based on decomposition and partial reconstruction of the $H_s$ time series once they have been characterized using wavelet analysis techniques. It was found that if the time series are treated accordingly, $H_s$ variations of $\pm 0.1$ m can be observed and therefore HF radar can provide the means to study the mechanisms responsible for the most significant energy variations in a particular wave field.

In particular, the filtered radar-derived observations were used to study the case of wind–sea propagating toward the coast line. It was found that, although the variations (RMS) in the energy field were small within the effective radar domain ($H_s \sim 0.2$ m), the radar was able to observe the energy trend. In a different case, where the filtered estimates were used to study wave growth under fetch-limited conditions, differences on the order of 0.05 m were observed. The treated data were also used to study the interaction of a wave field propagating against a strong surface current. In this case, a significant increase of wave height was observed in the region of wave–current interaction, offering evidence of the presence of wave shoaling effects.

In lieu of these results, it can be concluded that properly treated radar-derived estimates allow an adequate localization of regions of high concentration of energy and the identification of growth and attenuation tendencies of the energy in the wave field. Although additional measurements are necessary to draw more definitive quantitative conclusions, the good data correlation found encourages future work to further validate the methodology under similar and additional conditions and, if possible, with an independent wide-area measuring technique [such as synthetic aperture radar (SAR) imagery].

*Acknowledgments.* The experimental data used in this work were acquired by the Radar Ocean Sensing Laboratory of the University of Miami with the support of the Office of Naval Research (ONR). Grants were part of the ONR Remote Sensing Program under Contracts N00014-94-1-1016 and N00014-96-1-1065 and the Coastal Dynamics Branch under Contract N00014-97-1-0348. The authors are grateful to Lynn K. (Nick) Shay, Mark A. Donelan, and Susanne Lehner for their review and insightful comments during the development of this study. We also acknowledge the contribution of unknown reviewers that helped to improve the quality of the manuscript.

## REFERENCES


Barrick, D. E., 1971a: Theory of HF and VHF propagation across the rough sea, 1, The effective surface impedance for a slightly rough highly conducting medium at grazing incidence. *Radio Sci.,* **6,** 517–526.

——, 1971b: Theory of HF and VHF propagation across the rough sea, 2, Application to HF and VHF propagation above the sea. *Radio Sci.,* **6,** 527–533.

——, 1971c: Dependence of second-order sidebands in HF sea echo upon sea state. *Proc. Antennas and Propagation Int. Symp.,* Los Angeles, CA, Institute of Electrical and Electronics Engineers, 194–197.

——, 1972: First-order theory and analysis of MF/HF/VHF scatter from the sea. *IEEE Trans. Antennas Propag.,* **20,** 2–10.

——, 1977a: Extraction of wave parameters from measured HF radar sea-echo doppler spectra. *Radio Sci.,* **12,** 415–424.

——, 1977b: The ocean waveheight nondirectional spectrum from inversion of the HF sea-echo Doppler spectrum. *Remote Sens. Environ.,* **6,** 201–227.

Bouws, E., H. Günther, W. Rosenthal, and C. L. Vincent, 1985: Similarity of the wind wave spectrum in finite depth water 1. Spectral form. *J. Geophys. Res.,* **90,** 975–986.

——, ——, ——, and ——, 1987: Similarity of the wind wave spectrum in finite depth water – Part 2. Statistical relations between shape and growth stage parameters. *Dtsch. Hydrogr. Z.,* **40,** 24.

Cook, T. M., and L. K. Shay, 2002: Surface $M_2$ tidal currents along the North Carolina shelf observed with a high-frequency radar. *J. Geophys. Res.,* **107,** 3222, doi:10.1029/2002JC001320.

Dean, R. G., and R. A. Dalrymple, 1991: *Water Wave Mechanics for Engineers and Scientists*. 2nd ed. World Scientific, 353 pp.

Donelan, M. A., 1987: The effect of swell on the growth of wind waves. *Johns Hopkins APL Tech. Dig.,* **8,** 18–23.

——, W. M. Drennan, and A. K. Magnusson, 1996: Nonstationary analysis of the directional properties of propagating waves. *J. Phys. Oceanogr.,* **26,** 1901–1914.

Farge, M., 1992: Wavelet transforms and their applications to turbulence. *Annu. Rev. Fluid Mech.,* **24,** 395–457.

Foufoula-Georgiou, E., and P. Kumar, 1994: *Wavelets in Geophysics*. Academic Press, 384 pp.

Graber, H. C., and M. L. Heron, 1997: Wave height measurements from HF Radar. *Oceanography,* **10,** 90–92.

Hasselmann, K., and Coauthors, 1973: Measurements of wind-wave growth and swell decay during the Joint North Sea Wave Project (JONSWAP). *Dtsch. Hydrogr. Z.,* **8** (Suppl. A), 1–95.

Haus, B. K., 2007: Surface current effects on the fetch-limited growth of wave energy. *J. Geophys. Res.,* **112,** C03003, doi:10.1029/2006JC003924.

——, H. C. Graber, L. K. Shay, and T. M. Cook, 2003: Alongshelf variability of a coastal buoyancy current during the relaxation of downwelling favorable winds. *J. Coast. Res.,* **19,** 409–420.

——, J. D. Wang, J. Martinez-Pedraja, and N. Smith, 2004: Southeast Florida shelf circulation and volume exchange, observations of Km-Scale variability. *Estuarine Coastal Shelf Sci.,* **59,** 277–294.

——, R. J. Ramos, H. C. Graber, L. K. Shay, and Z. R. Hallock, 2006: Remote observation of the spatial variability of surface waves interacting with an estuarine outflow. *IEEE J. Oceanic Eng.,* **31,** 835–849.

Heron, M. L., P. E. Dexter, and B. T. McGann, 1985: Parameters of the air–sea interface by high-frequency ground-wave doppler radar. *Aust. J. Mar. Freshwater Res.,* **36,** 655–670.

Heron, S. F., and M. L. Heron, 1998: A comparison of algorithms for extracting significant wave height from HF radar ocean backscatter spectra. *J. Atmos. Oceanic Technol.,* **15,** 1157–1163.

Lindsay, R. W., D. B. Percival, and A. Rothrock, 1996: The discrete wavelet transform and the scale analysis of the surface properties of sea ice. *IEEE Trans. Geosci. Remote Sens.,* **34,** 711–787.

Liu, P. C., 1994: Wavelet spectrum analysis and ocean wind waves. *Wavelets in Geophysics,* E. Foufoula-Georgiou and P. Kumar, Eds., Academic Press, 151–166.

——, and G. C. Miller, 1996: Wavelet transforms and ocean current data analysis. *J. Atmos. Oceanic Technol.,* **13,** 1090–1099.

Maresca, J. W., Jr., and T. M. Georges, 1980: Measuring rms wave height and the scalar ocean wave spectrum with HF skywave radar. *J. Geophys. Res.,* **85,** 2759–2771.

Markin, M., 1995: Orthogonal wavelet analysis: Interannual variability in the sea surface temperature. *Bull. Amer. Meteor. Soc.,* **76,** 2179–2186.

Ramos, R. J., 2001: Analysis of synthetic random shoaling gravity waves. Internal Rep., Radar Ocean Sensing Laboratory, University of Miami-RSMAS, 38 pp.

——, 2006: 2-D analysis of wave energy evolution using wavelet transforms. Ph.D. dissertation, RSMAS/Applied Marine Physics Department, University of Miami, 145 pp.

Shay, L. K., S. J. Lentz, H. C. Graber, and B. K. Haus, 1998: Current structure variations detected by HF radar and vector measuring current meters. *J. Atmos. Oceanic Technol.,* **15,** 237–256.

——, T. M. Cook, Z. R. Hallock, B. K. Haus, H. C. Graber, and J. Martinez, 2001a: The strength of the $M_2$ tide at the Chesapeake Bay mouth. *J. Phys. Oceanogr.,* **31,** 427–449.

——, ——, B. K. Haus, H. C. Graber, J. Martinez, and Z. R. Hallock, 2001b: Observed surface currents during the Chesapeake Bay outfall plume experiments. *Proc. First Int. Radio Wave Oceanography Workshop,* Timberline, OR, Office of Naval Research, 137–145.

Torrence, C., and G. P. Compo, 1998: A practical guide to wavelet analysis. *Bull. Amer. Meteor. Soc.,* **79,** 61–78.

Wyatt, L. R., 1997: The ocean wave directional spectrum. *Oceanography,* **10,** 85–89.

——, 2000: Limits to the inversion of HF radar backscatter for ocean wave measurement. *J. Atmos. Oceanic Technol.,* **17,** 1651–1665.

——, S. P. Thompson, and R. R. Burton, 1999: Evaluation of high frequency radar wave measurement. *Coastal Eng.,* **37,** 259–282.

——, and Coauthors, 2003: Validation and intercomparisons of wave measurements and models during the EuroROSE experiments. *Coastal Eng.,* **48,** 1–28.

——, G. Liakhovetski, H. C. Graber, and B. K. Haus, 2005: Factors affecting the accuracy of SHOWEX HF radar wave measurements. *J. Atmos. Oceanic Technol.,* **22,** 847–859.

Young, I. R., 1999: *Wind Generated Ocean Waves*. Vol. 2, 1st ed. Elsevier, 94 pp.